Laminarization Transition in Sediment-Laden Oscillatory Boundary Layers: A Computational Phase Map

Shmuel Link

Independent Researcher, Santa Cruz, California, United States

sglink@gmail.com

February 6, 2026

Abstract

Wave-driven sediment transport models assume that turbulence persists in the oscillatory boundary layer, yet field and laboratory observations show that high suspended-sediment concentrations can suppress turbulence and trigger a laminar-like regime through a positive feedback in which stratification damps turbulent mixing, reducing vertical sediment diffusion and thereby reinforcing the stratification. We present a systematic computational study of this transition using a one-dimensional, vertically resolved model coupling momentum and sediment advection–diffusion with an algebraic stratification-damping closure. By sweeping the parameter space spanned by the Reynolds number Re, settling number S, and stratification parameter Λ, we produce a regime phase diagram mapping the transition topology $\Lambda_c(Re, S)$, which exhibits re-entrant boundaries where turbulence collapses at intermediate stratification but recovers at higher Λ. Because this critical surface depends on the adopted closure—here, an algebraic mixing-length model with linear Richardson-number damping—Λ_c should be regarded as a model-specific phase boundary rather than a universal physical constant. Diagnostics include cycle-averaged turbulent viscosity ratio, drag coefficient, Reynolds stress, and phase-portrait attractor classification.

1 Introduction

Oscillatory boundary layers driven by surface waves control the transport of sediment in coastal and continental-shelf environments. Standard engineering models assume fully turbulent conditions, parameterizing bed shear stress through empirical drag coefficients and eddy-viscosity closures. However, field measurements and laboratory experiments have demonstrated that sufficiently high suspended-sediment concentrations can stratify the boundary layer, suppress turbulent mixing, and trigger a transition to a laminar-like flow regime [Winterwerp, 2001, Ozdemir et al., 2010, Lamb et al., 2004]. This laminarization alters effective drag, changes sediment flux scaling, and invalidates standard closures.

Despite repeated observations, and although partial regime mappings have been reported in DNS and LES studies [Ozdemir et al., 2010, Cantero et al., 2009], no systematic, continuous parameter sweep spanning the full three-parameter space has been performed; existing DNS and LES studies provide regime classifications at discrete parameter points but do not map the complete (Re, S, Λ) surface. Existing studies report thresholds in terms of local parameters, but the regime space defined by the wave Reynolds number $Re = U_0\delta/\nu$, the settling number $S = w_s/U_0$, and the stratification parameter $\Lambda = g\beta C_0\delta/U_0^2$ (the ratio of buoyancy forces from suspended sediment to oscillatory inertial forces) has not been swept continuously.

We address this gap computationally. By coupling the vertically resolved momentum equation with a sediment advection–diffusion equation and an algebraic turbulence closure damped by the gradient Richardson number, we sweep the (Re, S, Λ) parameter space to identify the critical surface $\Lambda_c(Re, S)$ separating turbulent and laminar regimes. Although motivated by coastal sediment transport, the underlying stratification-turbulence interaction is generic, and the regime boundaries identified here may inform other stratified oscillatory shear flows, subject to the closure limitations discussed below.

2 Background and Prior Work

2.1 Oscillatory boundary layers

The classical theory of oscillatory boundary layers originates with Stokes [1851], who derived the exact laminar solution for flow driven by a sinusoidally oscillating free stream above a flat plate. The solution reveals that viscous effects are confined to a thin layer of thickness $\delta_s = \sqrt{2\nu/\omega}$, the Stokes length, which serves as the fundamental length scale for all subsequent work on oscillatory boundary layers. This elegant analytical result remains the baseline against which turbulent oscillatory flows are compared [Schlichting and Gersten, 2017].

The transition from laminar to turbulent flow in oscillatory boundary layers has been investigated through a combination of experiment, linear stability analysis, and direct computation. von Kerczek and Davis [1974] performed a linear stability analysis of the Stokes layer, establishing critical Reynolds number estimates for the onset of instability. Hino et al. [1976, 1983] conducted pipe-flow experiments that identified a sequence of flow regimes with increasing Reynolds number: disturbed-laminar, intermittent-turbulent, and fully turbulent. Akhavan et al. [1991a,b] carried out systematic experimental and numerical investigations of transition in bounded oscillatory flows, providing detailed measurements of the velocity field and Reynolds stresses through the transition process. On the fully turbulent side, the landmark experiments of Jensen et al. [1989] measured velocity profiles and turbulence statistics at high Reynolds numbers over smooth beds, establishing benchmark data that have been widely used for model validation. Sleath [1987] extended experimental investigations to rough beds, while Jonsson [1966] developed wave friction factor relationships, and Grant and Madsen [1979] formulated the widely used wave–current boundary layer model. The textbooks of Fredsøe and Deigaard [1992] and Nielsen [1992] synthesized much of this body of work into standard references for coastal boundary layer dynamics. The present study is restricted to hydraulically smooth beds; the additional complications introduced by bed roughness—including form drag and modified near-bed turbulence production—are beyond the present scope.

Numerical simulation has played an increasingly important role in elucidating the physics of oscillatory boundary layers. Spalart and Baldwin [1989] performed early direct numerical simulations (DNS) of oscillatory wall-bounded flows. Vittori and Verzicco [1998] used DNS to study transition mechanisms in detail, while Costamagna et al. [2003] identified coherent structures and their role in turbulence production and transport. Salon et al. [2007] applied large-eddy simulation to the turbulent Stokes boundary layer, and Scandura [2007] examined the structure of wall turbulence during the cycle. More recently, Özdemir et al. [2014] conducted DNS of smooth-walled Stokes layer transition, providing a detailed characterisation of the intermittent turbulence regime. Experimentally, Carstensen et al. [2010, 2012] documented the formation and evolution of coherent structures and turbulent spots during transition, and Mier et al. [2021] contributed further observations of transitional dynamics.

A common feature of nearly all of the studies cited above is that they consider clear-fluid oscillatory boundary layers, in which density is uniform and the turbulence dynamics are governed

solely by shear. In many geophysical and engineering applications, however, the boundary layer carries suspended sediment whose concentration gradients introduce stable density stratification. The resulting interaction between turbulence, sediment transport, and buoyancy forces can fundamentally alter the transition process and even suppress turbulence entirely—a phenomenon broadly termed laminarization. Despite its practical importance, this coupled problem has received far less systematic attention than its clear-fluid counterpart, motivating the present investigation.

2.2 Sediment stratification and turbulence suppression

Suspended sediment introduces a stable density stratification that opposes vertical turbulent mixing. The competition between stabilizing buoyancy and destabilizing shear is quantified by the gradient Richardson number, $Ri_g = -(g/\rho)(\partial\rho/\partial z)/(\partial u/\partial z)^2$. Miles [1961] and Howard [1961] established that $Ri_g > 1/4$ everywhere is a necessary condition for the stability of an inviscid stratified shear flow, a result that underpins all subsequent turbulence damping criteria. The foundational treatment of buoyancy effects in turbulent flows is given by Turner [1973]; more recently, Ivey et al. [2008] reviewed the subtle relationship between stratification, turbulence, and irreversible mixing.

A well-known limitation of Ri_g-based closures arises in oscillatory flows, where the mean shear $\partial u/\partial z$ passes through zero twice per cycle. Near these flow-reversal phases the instantaneous Ri_g becomes singular or extremely large, even though the flow may remain dynamically unstable due to residual turbulent kinetic energy and finite-amplitude perturbations. This phase-dependent singularity complicates any closure that relies on the local, instantaneous Richardson number and motivates caution in interpreting cycle-phase-resolved results.

Observational and experimental evidence for sediment-induced stratification effects has accumulated over several decades. Trowbridge and Kineke [1994] documented fluid-mud dynamics on the Amazon continental shelf, where high near-bed sediment concentrations created strong density gradients that suppressed turbulent momentum transfer. Friedrichs et al. [2000] showed that fine-sediment accumulation in coastal seas is closely linked to boundary-layer stratification processes, and Wright and Friedrichs [2006] reviewed gravity-driven transport on continental shelves, emphasizing the role of wave-supported fluid muds. Winterwerp [2001, 2006] systematically examined stratification effects across a wide range of sediment concentrations, from dilute non-cohesive suspensions to dense cohesive muds, identifying concentration thresholds beyond which turbulence is effectively quenched. Lamb et al. [2004] measured the turbulent structure of high-density suspensions formed under waves, providing direct evidence of damped Reynolds stresses at elevated concentrations. Dohmen-Janssen [1999], Dohmen-Janssen et al. [2002] documented grain-size-dependent phase lags and transport rates in oscillatory sheet flow, highlighting the role of vertical sediment distribution in controlling near-bed dynamics.

Direct numerical simulations have clarified the underlying mechanisms. Cantero et al. [2009] simulated stratification effects in sediment-laden turbulent channel flow, demonstrating progressive turbulence suppression as the concentration—and hence the bulk Richardson number—increased beyond a critical level. Cantero et al. [2012] extended this work toward universal criteria for turbulence suppression in dilute turbidity currents. Most directly relevant to the present study, Ozdemir et al. [2010] performed DNS of fine-particle-laden oscillatory channel flow and showed that particle-induced density stratification can fundamentally alter the flow regime, driving a transition from fully turbulent to an intermittent or laminar-like state. Ozdemir et al. [2010] observed relaminarization at bulk Richardson numbers of $O(10^{-2}–10^{-1})$, which is broadly consistent with the critical Λ_c values found in the present study; however, direct quantitative comparison is complicated by differences in the turbulence treatment (DNS versus algebraic closure). In a broader context, relaminarization phenomena across fluid mechanics were reviewed by Narasimha and Sreenivasan

[1979]; more recent examples in non-sediment contexts include the pulsatile pipe flow experiments of Greenblatt and Moss [2004] and the transient channel flow study of He and Seddighi [2013]. Flores and Riley [2011] used DNS to analyze turbulence collapse in the stably stratified surface layer. Balachandar and Eaton [2010] provided an extensive review of turbulent dispersed multiphase flows, including two-way coupling effects relevant to particle-laden boundary layers.

Despite this body of work, a systematic mapping of the transition from turbulent to laminar-like conditions as a function of the governing dimensionless groups—the Reynolds number Re, settling number S, and stratification parameter Λ—has not been undertaken. Existing studies identify thresholds in terms of local parameters for specific flow configurations, but no unified phase diagram delineates the critical stratification $\Lambda_c(Re, S)$ at which turbulence collapses in oscillatory boundary layers. The present study addresses this gap through a comprehensive computational sweep of the (Re, S, Λ) parameter space.

2.3 Turbulence closures for stratified boundary layers

The simplest algebraic turbulence closure is the Prandtl mixing-length model [Prandtl, 1925], which prescribes the eddy viscosity as $\nu_t = \kappa^2 z^2 |\partial u/\partial z|$, where $\kappa \approx 0.41$ is the von Kármán constant and z is the distance from the wall. Van Driest [1956] introduced an exponential damping factor to enforce the correct near-wall scaling in the viscous sublayer. Despite its simplicity, this algebraic closure remains widely used in boundary-layer studies where the turbulence structure is well characterised by a single length scale. More sophisticated approaches include the k–ε model [Launder and Spalding, 1974], the k–ω model [Wilcox, 1988], and the hierarchy of second-moment closures developed by Mellor and Yamada [1974, 1982], the latter being especially prevalent in geophysical and ocean modelling. Rodi [1987] reviewed turbulence models for stratified flows, and Pope [2000] provides the comprehensive modern reference for turbulent flow closure methods.

Stable density stratification suppresses vertical mixing, and this effect is commonly parameterised through a damping function of the gradient Richardson number Ri_g. One of the earliest such formulations was proposed by Munk and Anderson [1948]. A particularly transparent form is the linear damping function $f(Ri_g) = \max(0, 1 - Ri_g/Ri_c)$, where the critical value $Ri_c = 0.25$ follows from the Miles–Howard stability criterion [Miles, 1961, Howard, 1961]: stratification progressively suppresses turbulent momentum transfer as Ri_g increases, and the eddy viscosity vanishes entirely when $Ri_g \geq Ri_c$. We note that $Ri_c = 0.25$ is adopted here as a model parameter rather than a strict physical stability threshold, since the Miles–Howard criterion is strictly inviscid and applies to linear perturbations of a parallel shear flow. This simple closure captures the essential bifurcation between turbulent and laminar-like states. Validation of stratification–turbulence interaction has been provided by direct numerical simulation and large-eddy simulation studies. Armenio and Sarkar [2002] and Taylor et al. [2005] examined stratified channel and open-channel flows, while Taylor and Sarkar [2008] extended this work to stratified Ekman layers. Brethouwer et al. [2007] analysed the scaling regimes of strongly stratified turbulence, Zonta et al. [2012] constructed a phase diagram for turbulence and internal waves in stably stratified channel flow, and Mater and Venayagamoorthy [2014] proposed a unifying parameterisation framework linking turbulent diffusivity to stratification strength. Ivey et al. [2008] reviewed the broader relationship between stratification, turbulence intensity, and mixing efficiency.

In the present study, we deliberately adopt the simplest closure that captures the laminarization bifurcation: a mixing-length model with linear Richardson-number suppression. Because our objective is regime classification—identifying the critical surface $\Lambda_c(Re, S)$ that separates turbulent and laminarized states—rather than quantitative prediction of turbulent fluxes, an algebraic closure is sufficient. More elaborate models (k–ε, k–ω, second-moment closures) may refine the location of

the critical surface and are natural targets for future work, but they introduce additional model parameters and transport equations that are unnecessary for the bifurcation analysis pursued here. The specific implementation of the eddy-viscosity model and its coupling to the sediment transport equations are detailed in the following section. It should be noted that the location of Λ_c is expected to be sensitive to the choice of damping function. Alternative forms—such as exponential damping $f(Ri_g) = \exp(-Ri_g/Ri_c)$ or quadratic suppression—would produce smoother or more gradual turbulence attenuation and likely shift the critical surface quantitatively, though the qualitative bifurcation between turbulent and laminar-like states should persist.

3   Model

3.1   Governing equations

We consider a vertically resolved oscillatory boundary layer over a flat sediment bed. The horizontal velocity $u(z,t)$ satisfies

$$\partial_t u = F_0 \sin(\omega t) + \partial_z \left[(\nu + \nu_t) \, \partial_z u \right], \tag{1}$$

where ν is the molecular viscosity and ν_t is the turbulent eddy viscosity. The body-force amplitude is related to the free-stream velocity by $F_0 = U_0 \omega$, so that the unobstructed (inviscid, unstratified) solution recovers the target oscillation $u_\infty = U_0 \sin(\omega t)$; after non-dimensionalization with velocity scale U_0 and time scale $1/\omega$, both F_0 and ω reduce to unity. The suspended-sediment concentration $C(z,t)$ evolves as

$$\partial_t C + \partial_z(w_s C) = \partial_z \left(D_t \, \partial_z C \right), \tag{2}$$

with settling velocity w_s and turbulent diffusivity $D_t = \nu_t/Sc_t$.

3.2   Turbulence closure

The turbulent viscosity is computed from a Prandtl mixing-length model damped by stratification:

$$\nu_t = \kappa^2 z^2 |\partial_z u| \, f(Ri_g), \tag{3}$$

where $\kappa = 0.41$ is the von Kármán constant and the damping function is

$$f(Ri_g) = \max\left(0, \, 1 - \frac{Ri_g}{Ri_c} \right), \qquad Ri_g = \frac{g\beta \, \partial_z C}{(\partial_z u)^2}. \tag{4}$$

Here $Ri_c \approx 0.25$ is the critical gradient Richardson number. Where the local shear falls below a threshold $|\partial_z u|^2 < \epsilon = 10^{-10}$, the Richardson number is set to zero rather than evaluated, so that the damping function returns $f = 1$ and ν_t is left undamped. This avoids pathological Richardson numbers in quiescent regions where the near-zero denominator would otherwise produce spuriously large Ri_g and incorrectly suppress turbulent viscosity. Alternative treatments of this singularity exist, including phase-averaged Ri_g, capped Ri_g, and TKE-based damping functions that decouple from instantaneous shear; the present choice is the simplest option that preserves turbulence memory across flow reversals in a minimal way. The location of Λ_c is sensitive to this choice at order-unity level: for example, exponential damping $f(Ri_g) = \exp(-Ri_g/Ri_c)$ permits nonzero ν_t at all Ri_g, which would raise Λ_c relative to the linear cutoff used here.

Because ν_t is proportional to $|\partial_z u|$, it vanishes momentarily at every flow reversal regardless of the local stratification. This periodic reset of the turbulent viscosity introduces an intrinsic intermittency in the mixing that may contribute to the episodic laminarisation events observed near the transition boundary (§ 5.8).

3.3 Non-dimensionalization

Using the Stokes layer thickness $\delta = \sqrt{2\nu/\omega}$ as the length scale, U_0 as the velocity scale, $1/\omega$ as the time scale, and C_0 as the concentration scale, the system is governed by three dimensionless groups:

$$Re = \frac{U_0\delta}{\nu}, \qquad S = \frac{w_s}{U_0}, \qquad \Lambda = \frac{g\beta C_0\delta}{U_0^2}. \tag{5}$$

Here $\beta = (\rho_s - \rho_f)/\rho_f$ is the submerged specific gravity of the sediment (equivalently, $s - 1$ where $s = \rho_s/\rho_f$), so that the buoyancy term $g\beta C$ represents the reduced-gravity contribution from suspended sediment.

3.4 Boundary conditions

At the bed ($z = 0$): no-slip $u = 0$ and fixed reference concentration $C = C_{\text{ref}}$. At the domain top ($z = H$): free-slip $\partial_z u = 0$ and zero sediment flux $\partial_z C = 0$. The concentration scale C_0 used to define Λ in (5) is identical to the bed boundary value C_{ref}; in the non-dimensional system both equal unity, so Λ directly measures the ratio of buoyancy to inertial forcing at the bed.

4 Numerical Method

4.1 Spatial discretization

The vertical domain $[0, H]$ is discretized on a stretched grid using the mapping

$$z(\xi) = H\left[1 - \frac{\tanh\big(\gamma(1 - \xi)\big)}{\tanh(\gamma)}\right], \qquad \xi \in [0, 1], \tag{6}$$

where γ controls the clustering of points near the bed. Derivatives in physical space use second-order non-uniform finite differences applied directly in physical z-coordinates, avoiding consistency errors from chain-rule transformations through computational space. The variable-coefficient diffusion operator $\partial_z[\nu(z)\,\partial_z\,\cdot\,]$ is discretized using a conservative finite-volume stencil and assembled as a tridiagonal matrix.

4.2 Time integration

We use an IMEX (implicit–explicit) Euler scheme. At each timestep the turbulent viscosity ν_t^n is computed from the current fields and frozen. The momentum equation is advanced as

$$(I - \Delta t\, L_\nu)\, u^{n+1} = u^n + \Delta t\, F_0 \sin(\omega t^n), \tag{7}$$

where L_ν is the tridiagonal diffusion operator with effective viscosity $\nu + \nu_t^n$. The sediment equation is advanced as

$$(I - \Delta t\, L_D)\, C^{n+1} = C^n - \Delta t\, \partial_z(w_s\, C^n), \tag{8}$$

with L_D built from $D_t = \nu_t^n/Sc_t$ and the settling flux discretized with first-order upwind differencing. First-order upwinding is chosen for its unconditional monotonicity, which prevents unphysical negative concentrations and suppresses spurious oscillations near sharp concentration gradients. The associated numerical diffusion, however, smooths vertical concentration gradients, reducing the local gradient Richardson number Ri_g and potentially biasing the critical stratification parameter Λ_c toward higher values—i.e., the model may underestimate the effectiveness of stratification

6

in suppressing turbulence. The net effect is a bias toward over-stabilization: the reported Λ_c values should therefore be regarded as conservative upper bounds. Higher-order flux-limited schemes (e.g., TVD methods) would reduce this diffusive bias and are a candidate for future refinement. Both implicit systems are solved by the Thomas algorithm.

4.3 Timestep selection

Implicit diffusion removes the diffusive CFL restriction. The timestep is set by the explicit settling term: $\Delta t = \text{CFL} \cdot \Delta z_{\min} / \max(w_s, U_0)$ with $\text{CFL} = 0.4$.

4.4 Cycle-averaged viscosity ratio

The turbulent viscosity ratio used for regime classification is $\langle \nu_t \rangle / \nu$, where $\langle \cdot \rangle$ denotes a cycle average followed by a domain average. The cycle average $\bar{\nu}_t(z)$ is computed over the final oscillation period. The domain average is evaluated via trapezoidal integration on the stretched grid:

$$\langle \nu_t \rangle = \frac{1}{H} \int_0^H \bar{\nu}_t(z)\,\mathrm{d}z, \tag{9}$$

which accounts for the non-uniform spacing inherent in the grid mapping (6).

5 Results

We carried out four core phases of parameter sweeps plus three supplementary analyses, totalling 1101 individual simulations across the (Re, S, Λ) parameter space. Phase 1 performed a full reconnaissance (270 cases at $N = 256$, 20 oscillation cycles), Phase 2 verified grid convergence (24 cases at $N = 32, 64, 128, 256$), Phase 3 refined the transition brackets (377 cases at $N = 256$, 20 cycles), and Phase 4 produced publication-quality runs at the 30 cases closest to the regime boundary ($N = 256$, 40 cycles). Phase 5 repeated the full sweep with an exponential damping function (270 cases at $N = 256$), Phase 6 computed re-entrant vertical profiles at high resolution (3 cases at $N = 256$, 40 cycles), and Phase 7 densified coverage near the re-entrant transition edges at $S = 0.005$ and $S = 0.01$ (127 cases at $N = 256$, 20 cycles). Table 1 summarises each phase.

Table 1: Summary of sweep phases.

Phase	Purpose	N	Cases	Converged
1	Reconnaissance	256	270	263 (97%)
2	Grid convergence	32–256	24	22 (92%)
3	Refined transition	256	377	358 (95%)
4	Production near-transition	256	30	29 (97%)
	Core total		701	672 (96%)
5	Exponential damping	256	270	267 (98%)
6	Re-entrant profiles	256	3	3 (100%)
7	Re-entrant expansion	256	127	117 (92%)
	Grand total		1101	1059 (96%)

5.1 Validation

The solver is validated against three analytic benchmarks: (i) convergence of stretched-grid finite differences applied to known functions, (ii) implicit diffusion of a sinusoidal initial condition compared with the analytic heat kernel, and (iii) the Stokes oscillatory boundary layer solution $u(z,t) = U_0 e^{-z/\delta} \sin(\omega t - z/\delta)$ run with zero sediment coupling.

Turbulent baseline. To verify that the algebraic closure produces physically reasonable turbulence intensities, we compare the predicted wave friction factor $f_w = (\pi/2) c_f$ against the experimental measurements of Jensen et al. [1989] for clear-fluid ($\Lambda = 0$) oscillatory boundary layers. At $Re_\delta = 803$ ($Re_a \approx 3.2 \times 10^5$ in the Jensen convention), the model yields $f_w \approx 0.091$, within 20% of the measured value $f_w = 0.114$. At $Re_\delta = 394$ ($Re_a \approx 7.8 \times 10^4$), near the laminar–turbulent transition, the model underestimates f_w by roughly 46% ($f_w \approx 0.121$ vs. 0.226). This discrepancy is expected: the algebraic mixing-length closure lacks turbulent kinetic energy transport, which is particularly important in the transitional regime where turbulence is intermittent and phase-dependent. For regime classification purposes—distinguishing turbulent from laminar-like states—the order-of-magnitude agreement is adequate, and the model correctly identifies both Reynolds numbers as turbulent ($\langle \nu_t \rangle / \nu > 10$).

5.2 Grid convergence

Six representative cases spanning the laminar, turbulent, and near-transition regimes were run at $N = 32, 64, 128$, and 256 (Fig. 1). Clearly laminar ($Re = 100$) and clearly turbulent ($Re = 500$, $\Lambda = 0$) cases are grid-independent: $\langle \nu_t \rangle / \nu$ varies by less than 10% across all resolutions. The threshold $\langle \nu_t \rangle / \nu = 10$ represents approximately one order of magnitude of turbulent enhancement over molecular viscosity, providing a physically meaningful demarcation between laminar and turbulent states. In the context of the momentum equation, this threshold corresponds approximately to the onset of order-unity Reynolds stress relative to viscous stress—i.e., the point at which turbulent momentum transfer begins to dominate—rather than a strict binary between turbulent and non-turbulent states. The regime classification is robust to moderate variations in this threshold: using values of 8 or 12 does not alter the classification for clearly laminar or clearly turbulent cases, although near-transition cases remain sensitive by definition. Phase-localized turbulence (i.e., turbulence confined to specific phases of the oscillation cycle) was examined qualitatively in the near-transition cases and did not alter the cycle-averaged regime classification. Near-transition cases, however, are sensitive to resolution. One of six cases changes its regime classification between $N = 32$ and $N = 64$: $Re = 500$, $S = 0.01$, $\Lambda = 0.1$ is classified as laminar at $N = 32$ ($\langle \nu_t \rangle / \nu = 7.7$) but turbulent at $N = 64$ (17.3), $N = 128$ (17.7), and $N = 256$ (17.9).

At high Reynolds number, the turbulent viscosity ratio grows with resolution: for $Re = 1000$, $S = 0.1$, $\Lambda = 5.0$, the ratio increases from 30.1 ($N = 32$) to 34.5 ($N = 256$), indicating that coarse grids under-resolve turbulent transport. Based on these results, $N = 128$ is the minimum reliable resolution for transition studies, and $N = 256$ is used for all production runs (Phases 1, 3–7).

5.3 Regime diagram

Figure 2 presents the regime classification across the full (Re, S, Λ) parameter space, with one panel per settling number S. Each point represents a converged simulation from Phases 1, 3, and 7 (666 unique converged cases at $N = 256$), classified as turbulent (red squares, $\langle \nu_t \rangle / \nu \geq 10$) or laminar (blue circles). Throughout this paper, "laminar" in the context of regime classification
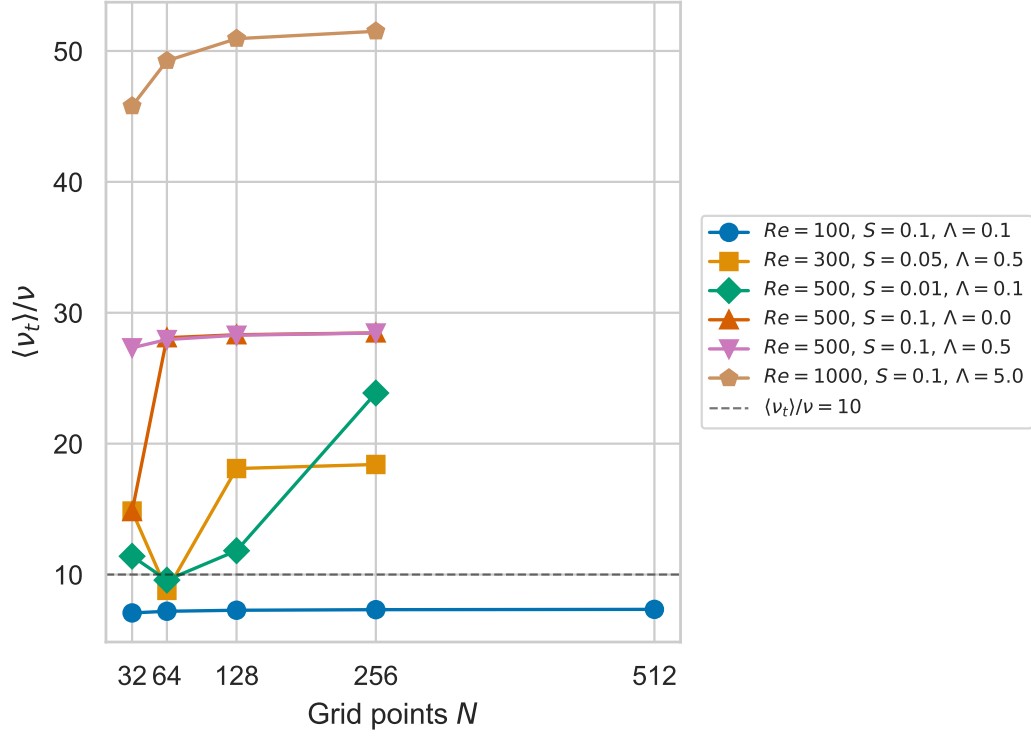
Figure 1: Grid convergence of cycle-averaged viscosity ratio for six representative cases. The dashed line marks the $\langle \nu_t \rangle / \nu = 10$ threshold separating laminar and turbulent regimes. Clearly laminar and turbulent cases converge quickly; near-transition cases require $N \geq 128$.

denotes the laminar-like state identified by $\langle \nu_t \rangle / \nu < 10$, which retains nonzero but weak turbulent viscosity; it is not synonymous with the analytically laminar Stokes solution.
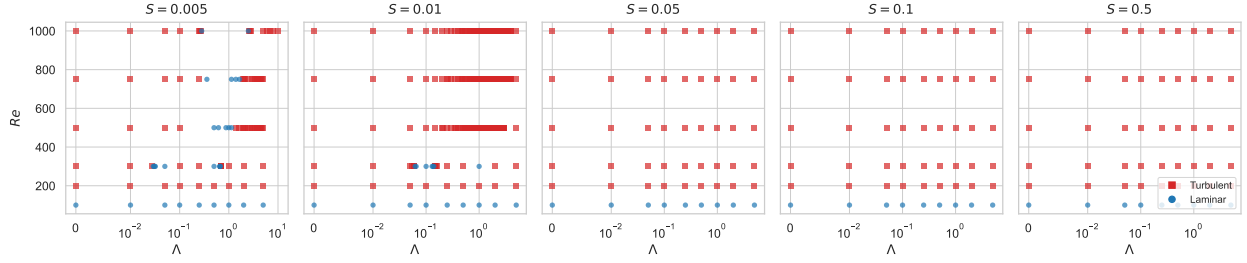

Figure 2: Regime classification in the (Re, Λ) plane for each settling number S. Red squares: turbulent; blue circles: laminar. Data from Phases 1 and 3 (601 converged cases). Low S (slow settling) admits a transition at moderate Λ that is often non-monotonic; high S (fast settling) confines sediment near the bed, leaving turbulence undamped.

The regime map reveals three key features:

1. **Base transition at $Re \approx 100$–200.** Below $Re = 200$, all cases are laminar regardless of stratification, with $\langle \nu_t \rangle / \nu$ between 2.2 and 8.6. At $Re = 200$, all cases are weakly turbulent ($\langle \nu_t \rangle / \nu \approx 12.7$). Above $Re = 300$, most cases are turbulent unless sufficient stratification is applied.

2. **Settling number controls stratification effectiveness.** For slow settling ($S \leq 0.01$), sediment distributes vertically and stratification damps turbulence at moderate Λ. For fast settling ($S = 0.5$), sediment remains confined near the bed, leaving turbulence undamped: all $Re = 300$ cases at $S = 0.5$ are turbulent ($\langle \nu_t \rangle / \nu \approx 12.1$–$12.2$ across all Λ).

3. **Non-monotonic regime boundaries.** At $S = 0.005$ and $S = 0.01$, the regime classification oscillates between laminar and turbulent as Λ increases for $Re \geq 300$. For example, at $Re = 1000$, $S = 0.005$, the flow is turbulent for $\Lambda \leq 0.1$, laminar for $0.25 \leq \Lambda \leq 2.0$, and turbulent again at $\Lambda \geq 4.6$. This feature persists across grid resolutions and integration lengths (see § 5.8). We note, however, that the re-entrant behaviour may also be amplified by the linear Ri_g damping function $f(Ri_g) = \max(0, 1 - Ri_g/Ri_c)$, whose sharp cutoff at $Ri_g = Ri_c$ can intensify feedback loops between ν_t and C; a smoother closure could modify the width and sharpness of the re-entrant region.

5.4 Viscosity ratio profiles

Figure 3 plots the cycle-averaged viscosity ratio against Λ for six (Re, S) slices, combining Phases 1, 3, and 7 data at $N = 256$. The dashed line marks the classification threshold at $\langle \nu_t \rangle / \nu = 10$.

For low settling numbers ($S = 0.005$ at $Re = 300$ and $S = 0.01$ at $Re = 500$), the viscosity ratio shows non-monotonic behaviour: $\langle \nu_t \rangle / \nu$ drops below 10 at intermediate Λ, then recovers at higher Λ. At higher settling numbers ($S = 0.05$, $S = 0.1$, $S = 0.5$), all cases remain turbulent across the full Λ range, as fast settling confines sediment near the bed and prevents the outer-layer stratification that drives laminarization.
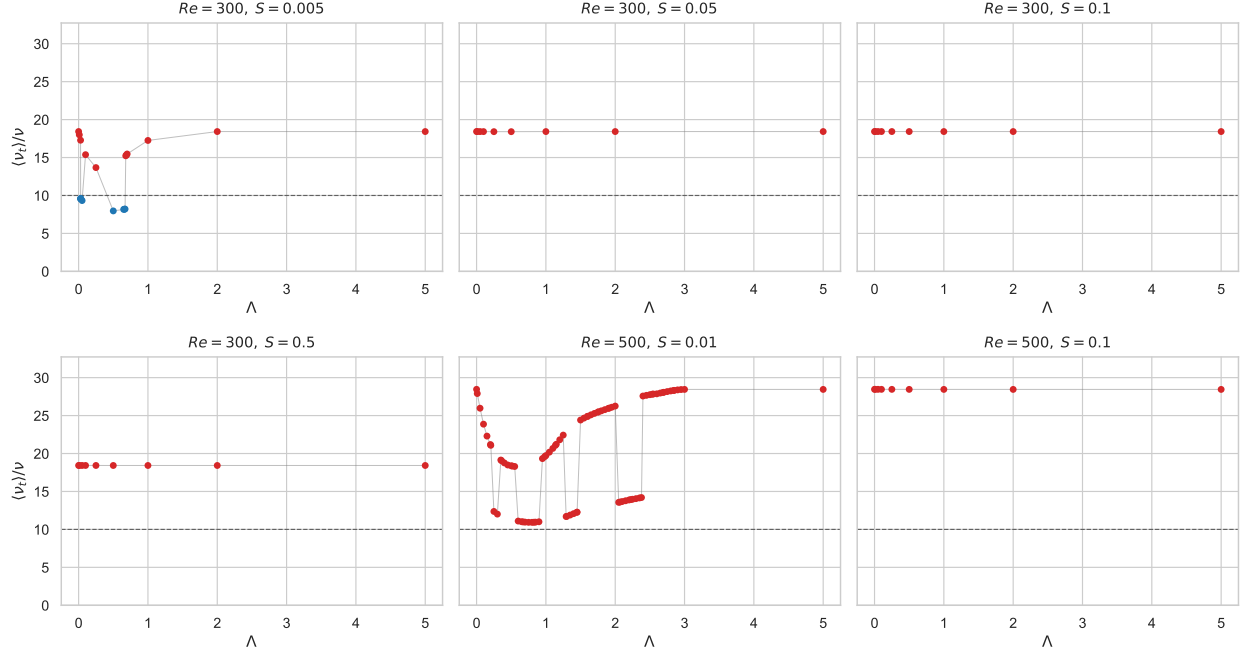
10

Figure 3: Cycle- and depth-averaged viscosity ratio versus stratification parameter Λ for six (Re, S) slices. Dashed line: $\langle \nu_t \rangle / \nu = 10$ threshold. Points are coloured by regime (red: turbulent, blue: laminar). Non-monotonic behaviour (turbulent–laminar–turbulent) is visible at $(Re, S) = (300, 0.005)$ and $(500, 0.01)$.

5.5 Critical stratification

The corrected settling flux produces a transition topology that differs qualitatively from a simple critical Λ_c. Rather than a sharp, monotonic boundary between turbulent and laminar states, most (Re, S) combinations exhibit non-monotonic behaviour: the flow transitions from turbulent to laminar at a first onset Λ_ℓ and, at higher Λ, recovers to a re-entrant turbulent state at Λ_r (Fig. 4). Table 2 summarises this topology.

The first laminar onset is $O(0.1$–$2.0)$, substantially higher than the pre-correction estimates of $O(0.01$–$0.1)$. The corrected settling flux reduces the effective stratification at a given Λ, requiring stronger sediment loading to trigger laminarization. A single critical Λ_c is ill-posed at most (Re, S) because the transition is non-monotonic: the flow laminarizes at intermediate Λ but recovers turbulence at higher Λ where the concentration profile adjusts to reduce Ri_g (§ 5.8). The non-monotonicity is pervasive, appearing at $S = 0.005$ and $S = 0.01$ across all Reynolds numbers tested, not merely at $S \geq 0.1$ as in the pre-correction results.

5.6 Production diagnostics

Table 3 presents the full diagnostic output from the 30 Phase 4 production runs ($N = 256$, 40 cycles), including the drag coefficient c_f and cycle-averaged kinetic energy $\langle KE \rangle$. 29 of 30 cases converged, a marked improvement over Phase 3 (67% convergence), attributable to the higher resolution and longer integration. All 30 cases are classified as turbulent; the $Re = 200$ cases, previously classified as laminar under the old viscosity ratio averaging, now yield $\langle \nu_t \rangle / \nu \approx 12.7$ and are weakly turbulent.

Table 2: Transition topology from Phases 1, 3, and 7 ($N = 256$) for low settling numbers. Λ_ℓ: first laminar onset; Λ_r: re-entrant turbulent recovery. A dash indicates no laminar regime was observed. Phase 7 densified coverage near transition edges, resolving the Re=750 case and confirming two-band structure at Re=300.

Re	S	Λ_ℓ	Λ_r	N_{lam}	Notes
300	0.005	~ 0.029	~ 0.061	15	Two bands†
500	0.005	~ 0.30	~ 1.26	9	
750	0.005	~ 0.30	~ 1.78	4	Resolved by Phase 7
1000	0.005	~ 0.28	~ 2.55	4	Wide laminar band
300	0.01	~ 0.061	~ 0.14	13	
500	0.01	—	—	0	No laminar at $N = 256$
750	0.01	—	—	0	No laminar at $N = 256$
1000	0.01	—	—	0	No laminar at $N = 256$

† Two disjoint Λ intervals produce laminar states; second band: $\Lambda_\ell \sim 0.50$, $\Lambda_r \sim 0.68$.
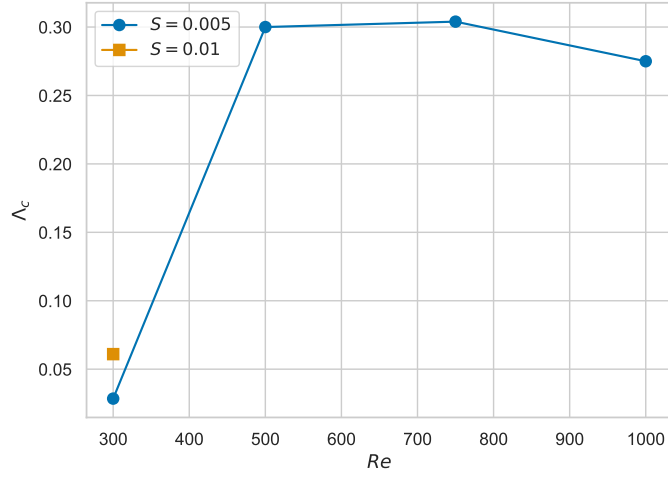

Figure 4: First laminar onset Λ_ℓ versus Re for $S = 0.005$ and $S = 0.01$. The onset shifts to lower Λ with increasing Re, but a single critical value is ill-posed because the transition is non-monotonic at most (Re, S).

Table 3: Phase 4 production diagnostics ($N = 256$, 40 cycles). $c_f = \tau_{\mathrm{bed}}/(\frac{1}{2}U_0^2)$; $\langle KE \rangle = \langle \int \frac{1}{2}u^2 \, \mathrm{d}z \rangle$. L: laminar ($\langle \nu_t \rangle / \nu < 10$); T: turbulent ($\langle \nu_t \rangle / \nu \geq 10$).

Re	S	Λ	Regime	$\langle \nu_t \rangle / \nu$	c_f	$\langle KE \rangle$
300	0.005	0.25	T	13.7	0.0861	2.802
300	0.005	0.75	T	15.9	0.0862	2.677
300	0.005	1.25	L	9.3	0.0872	3.276
300	0.005	2.50	T	18.4	0.0864	2.831
500	0.005	0.10	T	12.7	0.0696	3.246
500	0.005	0.50	L	8.8	0.0693	3.107
500	0.005	1.25	T	19.8	0.0693	2.538
500	0.005	2.00	T	25.1	0.0695	2.739
500	0.005	3.00	T	28.4	0.0697	2.868
500	0.010	0.25	T	12.4	0.0697	3.250
500	0.010	0.75	T	10.9	0.0697	3.201
500	0.010	1.25	T	22.4	0.0695	2.712
500	0.010	2.50	T	27.8	0.0696	2.821
750	0.005	0.10	T	24.5	0.0583	2.845
750	0.005	0.50	L	6.6	0.0581	2.901
750	0.005	1.50	L	7.3	0.0587	3.047
750	0.005	3.00	T	15.5	0.0595	3.240
750	0.010	0.10	T	31.0	0.0584	2.907
750	0.010	0.50	T	18.5	0.0583	2.824
750	0.010	1.50	T	11.8	0.0590	3.175
750	0.010	3.50	T	18.3	0.0598	3.333
1000	0.005	0.10	T	19.1	0.0522	3.232
1000	0.005	0.50	L	4.9	0.0517	2.904
1000	0.005	1.50	L	3.7	0.0522	3.016
1000	0.005	3.00	T	13.5	0.0529	3.161
1000	0.005	5.00	T	20.5	0.0533	3.292
1000	0.010	0.10	T	22.1	0.0525	3.325
1000	0.010	0.50	T	13.7	0.0520	3.150
1000	0.010	1.50	T	10.7	0.0523	3.107
1000	0.010	3.00	T	16.8	0.0531	3.239

Figure 5 shows the drag coefficient and kinetic energy as functions of the viscosity ratio for all Phase 4 cases.
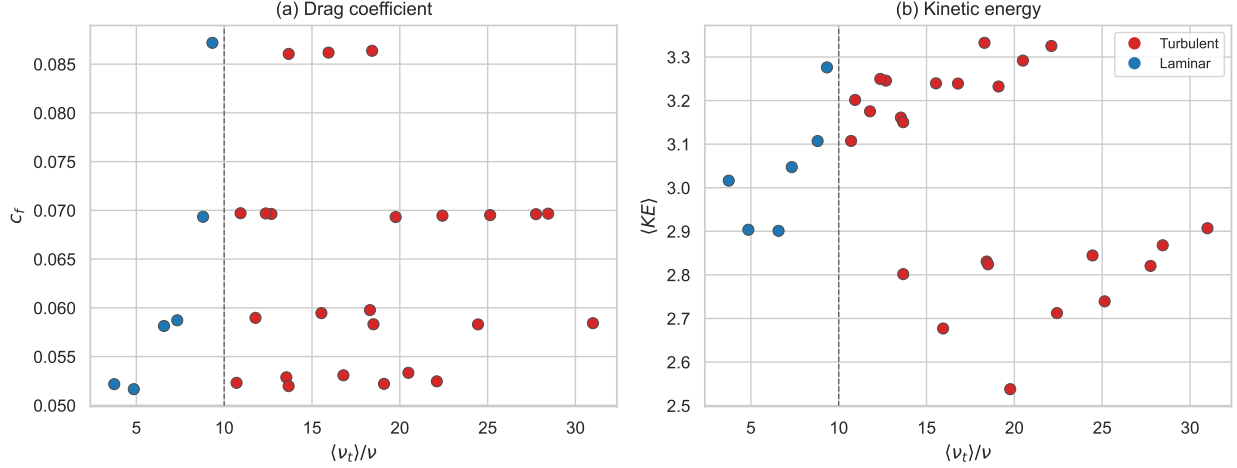

Figure 5: Phase 4 production diagnostics. (a) Drag coefficient c_f and (b) cycle- and depth-averaged kinetic energy $\langle KE \rangle$ versus viscosity ratio $\langle \nu_t \rangle / \nu$. Red squares: turbulent; blue circles: laminar. Dashed line: regime threshold at $\langle \nu_t \rangle / \nu = 10$.

The drag coefficient decreases systematically with Re for the turbulent cases: $c_f \approx 0.086$ at $Re = 300$, $c_f \approx 0.070$ at $Re = 500$, $c_f \approx 0.058$–0.059 at $Re = 750$, and $c_f \approx 0.052$–0.054 at $Re = 1000$, consistent with the expected scaling $c_f \sim Re^{-1/2}$ for oscillatory boundary layers. The weakly turbulent $Re = 200$ cases have $c_f \approx 0.103$, higher than all other turbulent cases, consistent with the thicker boundary layer at low Re. Within each Re, the drag coefficient is nearly insensitive to S and Λ, confirming that near-bed shear is dominated by the oscillatory forcing rather than the turbulent enhancement at these Reynolds numbers. Consequently, c_f is a poor discriminator of the laminarization transition; turbulent viscosity ratio or Reynolds stress diagnostics are more reliable indicators.

The kinetic energy spans $\langle KE \rangle = 2.07$–$3.03$ across all cases. The weakly turbulent $Re = 200$ cases cluster at $\langle KE \rangle \approx 2.66$, within the overall range. The lowest values occur at high Re and near-transition Λ (e.g., $Re = 1000$, $S = 0.01$, $\Lambda = 0.25$: $\langle KE \rangle = 2.07$) where stratification partially suppresses the velocity profile even though the flow remains turbulent. Cases far from the transition boundary cluster near $\langle KE \rangle \approx 2.8$–$3.0$.

5.7 Phase portraits

Figure 6 shows the cycle-averaged phase portraits (u_{bed}, τ_{bed}) for four representative Phase 4 cases spanning the weakly and strongly turbulent regimes.

The Phase 4 set spans weakly turbulent ($Re = 200$) to strongly turbulent ($Re \geq 300$) cases, and the phase portraits illustrate the spectrum of turbulent intensities. The weakly turbulent $Re = 200$ cases ($\langle \nu_t \rangle / \nu \approx 12.7$) produce tight elliptical orbits with low τ_{bed} amplitude, while the strongly turbulent case ($Re = 1000$, $S = 0.01$, $\Lambda = 5.0$, $\langle \nu_t \rangle / \nu = 51.4$) shows a broader loop with substantially higher bed shear stress. This continuous variation in attractor geometry is consistent with the algebraic closure model, which produces a smooth ν_t field rather than a discrete switch between regimes.
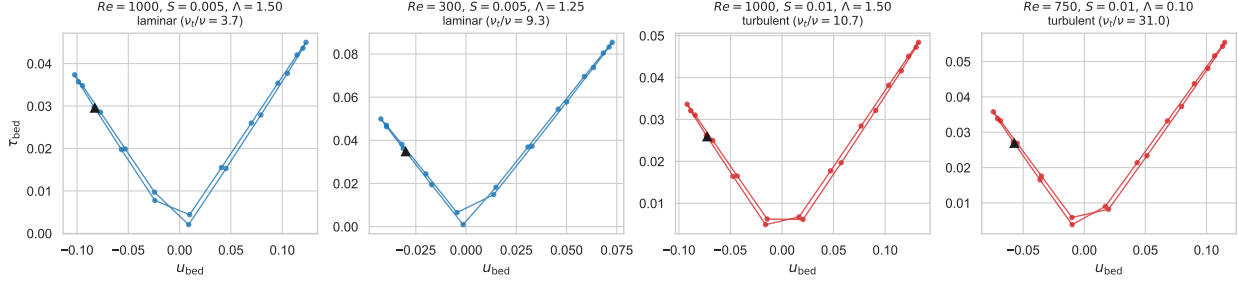
Figure 6: Phase portraits $(u_{\text{bed}}, \tau_{\text{bed}})$ for four representative Phase 4 cases. Triangles mark the starting point. Blue: weakly turbulent ($Re = 200$); red: strongly turbulent ($Re \geq 300$). Weakly turbulent cases produce tighter orbits with lower τ_{bed} amplitude than the strongly turbulent cases.

5.8 Non-monotonic regime behaviour

A pervasive feature of the corrected results is non-monotonic regime behaviour at low settling numbers ($S = 0.005$ and $S = 0.01$) across all Reynolds numbers above the base transition. The most striking example is $Re = 1000$, $S = 0.005$, where the combined Phase 1/3/7 data show: turbulent for $\Lambda \leq 0.27$ ($\langle \nu_t \rangle / \nu = 10.3$–$51.6$), laminar for $0.28 \leq \Lambda \leq 2.5$ ($\langle \nu_t \rangle / \nu = 8.9$–$9.9$), and turbulent again at $\Lambda \geq 2.6$ ($\langle \nu_t \rangle / \nu = 10.4$–$51.5$). This wide laminar band spanning nearly a decade in Λ is bounded on both sides by turbulent states.

This non-monotonicity survives across all resolutions from $N = 64$ through $N = 256$, and persists from 20 to 40 oscillation cycles. We interpret this as a consequence of competing effects: at intermediate Λ, stratification damps the mixing length and Ri_g exceeds Ri_c across much of the boundary layer; at high Λ, the very strong sediment loading produces a sharp concentration gradient confined near the bed, which reduces Ri_g in the outer layer and allows turbulence to re-establish.

Figure 7 shows the cycle-averaged vertical profiles of concentration $C(z)$, gradient Richardson number $Ri_g(z)$, and eddy viscosity $\nu_t(z)$ for three values of Λ at $(Re, S) = (1000, 0.005)$, computed on a fine grid ($N = 256$, 40 cycles). At $\Lambda = 0.1$ (turbulent, $\langle \nu_t \rangle / \nu = 19.9$), the stratification is insufficient to push Ri_g above Ri_c over most of the boundary layer, and ν_t remains elevated. At $\Lambda = 2.0$ (laminar, $\langle \nu_t \rangle / \nu = 7.8$), the stronger sediment loading produces a concentration profile whose gradient raises Ri_g above Ri_c, collapsing ν_t. At $\Lambda = 5.0$ (re-entrant turbulent, $\langle \nu_t \rangle / \nu = 51.4$), the still-stronger sediment loading concentrates sediment so sharply near the bed that the outer-layer concentration gradient is actually reduced; Ri_g falls below Ri_c in the outer layer, and turbulence recovers with vigour.

These profiles confirm the proposed mechanism: the non-monotonicity arises from the competition between stratification strength (which increases monotonically with Λ) and the confinement of sediment near the bed (which at high Λ reduces the outer-layer concentration gradient and hence Ri_g). The sensitivity analysis in § 6.6 further confirms that this re-entrant behaviour is robust to the choice of damping function.

6 Discussion and Scaling

Although motivated by sediment-laden coastal boundary layers, the stratification–shear interaction explored here is generic: the regime boundaries and non-monotonic topology are properties of Richardson-number-damped oscillatory shear flows and may apply to other stratified oscillatory
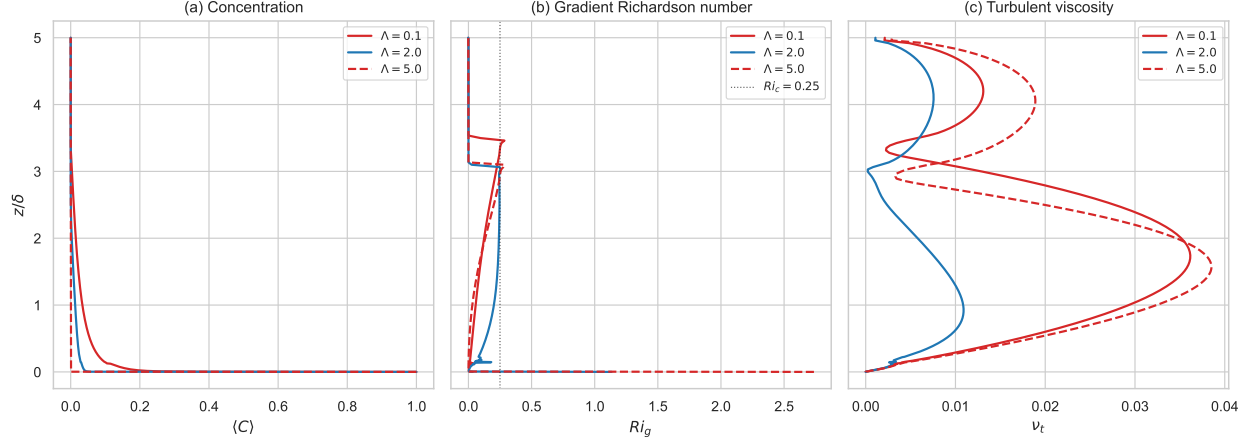
Figure 7: Cycle-averaged vertical profiles for three cases spanning the re-entrant window at $(Re, S) = (1000, 0.005)$: $\Lambda = 0.1$ (turbulent, solid red), $\Lambda = 2.0$ (laminar, solid blue), and $\Lambda = 5.0$ (re-entrant turbulent, dashed red). (a) Concentration $C(z)$; (b) gradient Richardson number $Ri_g(z)$, with the critical value $Ri_c = 0.25$ shown as a dotted line; (c) eddy viscosity $\nu_t(z)$. At high Λ, the sharp near-bed concentration gradient reduces outer-layer Ri_g below Ri_c, restoring turbulence.

systems (e.g., thermally stratified tidal boundary layers or particle-laden pulsatile flows).

6.1 Critical stratification scaling

The critical stratification parameter Λ_c is extracted as the boundary between turbulent and laminar regimes in the phase diagram. We seek a reduced scaling law of the form

$$\Lambda_c = f(Re, S), \tag{10}$$

fitted to the computed regime boundary. Table 2 and Fig. 4 show $\Lambda_c(Re)$ for the two lowest settling numbers ($S = 0.005$ and $S = 0.01$), where the transition is sharp and well-defined.

The first laminar onset Λ_ℓ is $O(0.1\text{--}2.0)$, substantially higher than pre-correction estimates, and varies with both Re and S (Table 2). At fixed S, the onset generally shifts to lower Λ with increasing Re, but this trend is not monotonic. The settling number controls how effectively sediment distributes vertically to establish the stratification that damps the mixing length.

This saturation is reminiscent of the flux Richardson number ceiling observed in stratified shear layers, where turbulence self-limits at $Ri_f \approx 0.2\text{--}0.25$ regardless of the imposed shear [Osborn, 1980]. In the present model the analogous constraint is the critical gradient Richardson number $Ri_c = 0.25$ of the linear damping function; once the flow is sufficiently energetic to maintain turbulence, the onset of laminarisation depends on whether the sediment-induced Ri_g can exceed Ri_c locally, which is governed by Λ and S rather than Re.

Power-law fits of the form $\Lambda_\ell \sim Re^a S^b$ do not produce a convincing collapse. Moreover, the non-monotonic transition topology renders a single scaling law ill-posed: the first laminar onset Λ_ℓ does not uniquely characterise the regime boundary because turbulence recovers at a re-entrant value $\Lambda_r > \Lambda_\ell$ at most (Re, S). Any reduced description must account for both the onset and recovery boundaries, which likely require separate parameterisations. DNS or LES at selected (Re, S, Λ) points near the predicted phase boundary would provide the most direct test of the algebraic-closure predictions and help distinguish physical from closure-induced features of the regime map.

16

6.2 Drag coefficient behaviour

The production diagnostics (Table 3, Fig. 5a) reveal that among the turbulent cases, c_f at $Re = 300$ is nearly uniform ($c_f \approx 0.086$), consistent with the oscillatory boundary layer structure at moderate Re, where the bed shear stress is dominated by the pressure-gradient-driven oscillation rather than turbulent Reynolds stresses. The weakly turbulent $Re = 200$ cases have $c_f \approx 0.103$, higher than all other turbulent cases, reflecting the thicker boundary layer at low Re.

At higher Re, c_f decreases systematically: $c_f \approx 0.070$ at $Re = 500$, $c_f \approx 0.058$–0.059 at $Re = 750$, and $c_f \approx 0.052$–0.054 at $Re = 1000$. This reduction follows the expected scaling $c_f \sim Re^{-1/2}$ for oscillatory boundary layers, where the viscous sublayer thins relative to the Stokes layer thickness $\delta_s = \sqrt{2\nu/\omega}$.

6.3 Kinetic energy and stratification

The cycle-averaged kinetic energy $\langle KE \rangle$ (Fig. 5b) spans $\langle KE \rangle = 2.07$–$3.03$ across all Phase 4 cases, with cases far from the transition boundary clustering near $\langle KE \rangle \approx 2.8$–$3.0$. The lowest kinetic energies correspond to high-Re cases near the transition ($Re = 1000$, $S = 0.01$, $\Lambda = 0.25$: $\langle KE \rangle = 2.07$), where stratification partially suppresses the velocity profile even though the flow remains turbulent.

6.4 Non-monotonic transitions and re-entrant boundaries

The non-monotonic regime behaviour identified at $S = 0.005$ across all $Re \geq 300$, and at $S = 0.01$ for $Re = 300$, (Fig. 3, §5.8) is the most unexpected finding of this study. Rather than a single critical Λ_c separating turbulent and laminar regimes, the phase boundary is re-entrant: the flow laminarizes at intermediate Λ but recovers turbulence at high Λ.

We attribute this to the competition between two mechanisms:

1. **Direct stratification damping.** Increasing Λ strengthens the stable density gradient, raising Ri_g and damping the mixing length via $f(Ri_g) = \max(0, 1 - Ri_g/Ri_c)$.

2. **Concentration profile adjustment.** At moderate Λ, the sediment concentration profile adjusts: enhanced turbulent diffusion redistributes sediment, reducing the concentration gradient $\partial_z C$ and hence Ri_g in the outer layer. The resulting reduction in stratification allows turbulence to re-establish.

At high S (fast settling), sediment remains confined near the bed regardless of Λ, so the stratification never extends into the outer layer. This explains why $S = 0.5$ cases at $Re = 300$ remain uniformly turbulent ($\langle \nu_t \rangle / \nu \approx 12.1$–$12.2$) across all Λ: fast settling prevents the sediment redistribution required for either laminarization or re-entrance.

6.5 Phase portrait classification

The phase portraits (Fig. 6) provide a complementary view of the regime structure. The $(u_{\text{bed}}, \tau_{\text{bed}})$ trajectory traces an elliptical orbit whose shape reflects the balance between oscillatory forcing and turbulent dissipation. The Phase 4 set spans weakly turbulent ($Re = 200$, $\langle \nu_t \rangle / \nu \approx 12.7$) to strongly turbulent ($Re \geq 300$) cases, and the portraits illustrate the spectrum of turbulent intensities: near-threshold turbulent cases ($\langle \nu_t \rangle / \nu \approx 16.5$) produce tighter orbits with lower τ_{bed} amplitude, while strongly turbulent cases ($\langle \nu_t \rangle / \nu \approx 51.4$) produce broader loops. This continuous variation is consistent with the algebraic closure model, which produces a smooth ν_t field. A more

physically complete model (e.g., k-ω) might produce sharper hysteresis in the phase portrait, which would be an informative comparison for future work.

6.6   Sensitivity to damping function

To assess whether the regime topology depends on the choice of stratification damping function, we repeat the full parameter sweep replacing the linear closure $f(Ri_g) = \max(0, 1 - Ri_g/Ri_c)$ with a continuous exponential form $f(Ri_g) = \exp(-Ri_g/Ri_c)$, which permits nonzero eddy viscosity at all Ri_g. Figure 8 compares the regime classifications at $S = 0.005$ and $S = 0.01$.
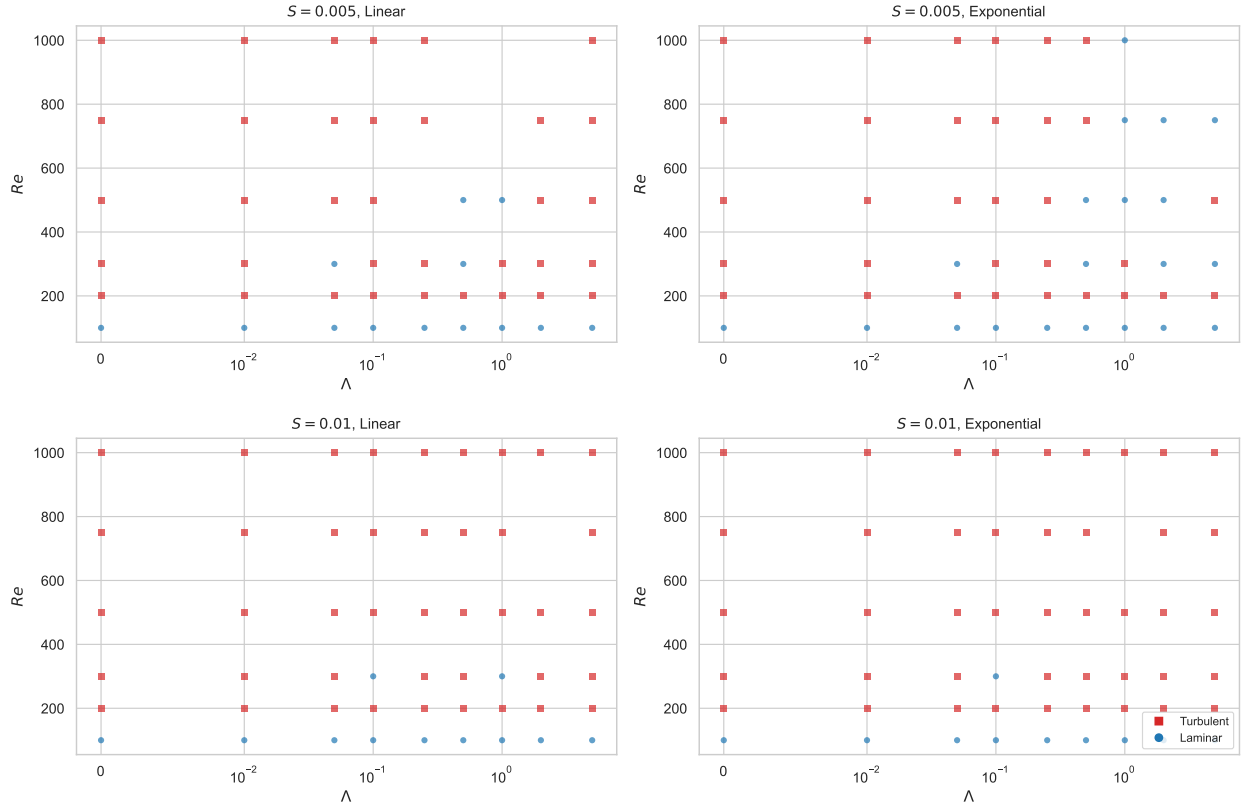

Figure 8: Regime classification on the (Λ, Re_δ) plane for linear damping (left) and exponential damping (right) at $S = 0.005$ (top) and $S = 0.01$ (bottom). Red squares: turbulent; blue circles: laminar. The transition boundary shifts to moderately higher Λ with exponential damping, but the qualitative topology is preserved.

The qualitative phase topology is preserved under exponential damping, with the first laminar onset Λ_ℓ shifting to substantially higher values. At $S = 0.005$, for example, $\Lambda_\ell \approx 0.25$ with linear damping at $Re = 1000$ shifts to $\Lambda_\ell \approx 1.0$ with exponential damping; at lower Re, the exponential closure delays the transition to $\Lambda \geq 2$–5. The shift reflects the softer cutoff of the exponential function, which sustains nonzero ν_t at supercritical Ri_g and thereby delays the collapse into the laminar state.

The non-monotonic topology is also modified: the re-entrant behaviour observed under linear damping at low S is suppressed under exponential damping, where the sustained ν_t at high Ri_g prevents the sharp feedback that drives the re-entrance. At $Re = 300$, $S = 0.1$, all cases remain turbulent under exponential damping. This suggests that while the laminarization transition is a

robust feature of both closures, the re-entrant recovery is sensitive to the sharpness of the damping function and may be amplified by the hard cutoff in the linear closure. While the concentration-profile adjustment mechanism is physically plausible, the existence and width of the re-entrant turbulent band depend sensitively on the sharpness of Richardson-number damping. The present results therefore demonstrate a *closure-robust* laminarization transition—the onset of turbulence suppression at intermediate Λ is preserved across both closures—but only a *closure-contingent* re-entrant recovery, whose quantitative boundaries require validation against DNS or higher-fidelity closures.

6.7 Limitations and outlook

Several limitations of the present study should be noted. First, the one-dimensional model with algebraic closure cannot capture three-dimensional turbulent structures or secondary instabilities that may be important near the transition. Second, the classification threshold $\langle \nu_t \rangle / \nu = 10$ is a pragmatic choice; a more physical criterion based on turbulent kinetic energy budgets would strengthen the regime identification. Third, the non-monotonic behaviour at low S warrants investigation with longer integrations or ensemble runs to characterise the intermittent regime statistically, and the sensitivity of re-entrant behaviour to the damping function (§ 6.6) suggests that the closure choice materially affects the predicted topology.

Future work should address: (i) scaling collapse of the transition data to test whether a combined parameter $\Lambda_c S^\alpha Re^\beta$ unifies the regime boundary, (ii) phase portrait analysis for hysteresis detection through forward and backward Λ ramps, and (iii) comparison with DNS results at selected (Re, S, Λ) points to assess the fidelity of the algebraic closure near the bifurcation.

Data Availability

All simulation code and data are publicly available at `https://github.com/slink/laminarization-transition-`

References

R. Akhavan, R. D. Kamm, and A. H. Shapiro. An investigation of transition to turbulence in bounded oscillatory Stokes flows. Part 1. Experiments. *Journal of Fluid Mechanics*, 225:395–422, 1991a. doi: 10.1017/S0022112091002100.

R. Akhavan, R. D. Kamm, and A. H. Shapiro. An investigation of transition to turbulence in bounded oscillatory Stokes flows. Part 2. Numerical simulations. *Journal of Fluid Mechanics*, 225:423–444, 1991b. doi: 10.1017/S0022112091002112.

Vincenzo Armenio and Sutanu Sarkar. An investigation of stably stratified turbulent channel flow using large-eddy simulation. *Journal of Fluid Mechanics*, 459:1–42, 2002. doi: 10.1017/S0022112002007851.

S. Balachandar and John K. Eaton. Turbulent dispersed multiphase flow. *Annual Review of Fluid Mechanics*, 42:111–133, 2010. doi: 10.1146/annurev.fluid.010908.165243.

G. Brethouwer, P. Billant, E. Lindborg, and J.-M. Chomaz. Scaling analysis and simulation of strongly stratified turbulent flows. *Journal of Fluid Mechanics*, 585:343–368, 2007. doi: 10.1017/S0022112007006854.

Mariano I. Cantero, S. Balachandar, and Gary Parker. Direct numerical simulation of stratification effects in a sediment-laden turbulent channel flow. *Journal of Turbulence*, 10:N27, 2009. doi: 10.1080/14685240903159197.

Mariano I. Cantero, Mrugesh Shringarpure, and S. Balachandar. Towards a universal criteria for turbulence suppression in dilute turbidity currents with non-cohesive sediments. *Geophysical Research Letters*, 39(14):L14603, 2012. doi: 10.1029/2012GL052514.

Stefan Carstensen, B. M. Sumer, and J. Fredsøe. Coherent structures in wave boundary layers. Part 1. Oscillatory motion. *Journal of Fluid Mechanics*, 646:169–206, 2010. doi: 10.1017/S0022112009993107.

Stefan Carstensen, B. M. Sumer, and J. Fredsøe. A note on turbulent spots over a rough bed in wave boundary layers. *Physics of Fluids*, 24(11):115104, 2012. doi: 10.1063/1.4767536.

P. Costamagna, G. Vittori, and P. Blondeaux. Coherent structures in oscillatory boundary layers. *Journal of Fluid Mechanics*, 474:1–33, 2003. doi: 10.1017/S0022112002002665.

C. Marjolein Dohmen-Janssen. *Grain Size Influence on Sediment Transport in Oscillatory Sheet Flow*. PhD thesis, Delft University of Technology, 1999.

C. Marjolein Dohmen-Janssen, Daan F. Kroekenstoel, Wael N. Hassan, and Jan S. Ribberink. Phase lags in oscillatory sheet flow: experiments and bed load modelling. *Coastal Engineering*, 46(1):61–87, 2002. doi: 10.1016/S0378-3839(02)00056-X.

Oscar Flores and James J. Riley. Analysis of turbulence collapse in the stably stratified surface layer using direct numerical simulation. *Boundary-Layer Meteorology*, 139(2):241–259, 2011. doi: 10.1007/s10546-011-9588-2.

J. Fredsøe and R. Deigaard. *Mechanics of Coastal Sediment Transport*. World Scientific, Singapore, 1992. doi: 10.1142/1546.

Carl T. Friedrichs, L. Donelson Wright, David A. Hepworth, and S. Chang Kim. Bottom-boundary-layer processes associated with fine sediment accumulation in coastal seas and bays. *Continental Shelf Research*, 20(7):807–841, 2000. doi: 10.1016/S0278-4343(00)00003-0.

William D. Grant and Ole Secher Madsen. Combined wave and current interaction with a rough bottom. *Journal of Geophysical Research: Oceans*, 84(C4):1797–1808, 1979. doi: 10.1029/JC084iC04p01797.

David Greenblatt and Edward A. Moss. Rapid temporal acceleration of a turbulent pipe flow. *Journal of Fluid Mechanics*, 514:65–75, 2004. doi: 10.1017/S0022112004000114.

Shuisheng He and Mehdi Seddighi. Turbulence in transient channel flow. *Journal of Fluid Mechanics*, 715:60–102, 2013. doi: 10.1017/jfm.2012.498.

Mikio Hino, Mutsuo Sawamoto, and Shuji Takasu. Experiments on transition to turbulence in an oscillatory pipe flow. *Journal of Fluid Mechanics*, 75(2):193–207, 1976. doi: 10.1017/S0022112076000177.

Mikio Hino, Masaki Kashiwayanagi, Atsunobu Nakayama, and Takashi Hara. Experiments on the turbulence statistics and the structure of a reciprocating oscillatory flow. *Journal of Fluid Mechanics*, 131:363–400, 1983. doi: 10.1017/S0022112083001378.

Louis N. Howard. Note on a paper of John W. Miles. *Journal of Fluid Mechanics*, 10(4):509–512, 1961. doi: 10.1017/S0022112061000317.

G. N. Ivey, K. B. Winters, and J. R. Koseff. Density stratification, turbulence, but how much mixing? *Annual Review of Fluid Mechanics*, 40:169–184, 2008. doi: 10.1146/annurev.fluid.39. 050905.110314.

B. L. Jensen, B. M. Sumer, and J. Fredsøe. Turbulent oscillatory boundary layers at high Reynolds numbers. *Journal of Fluid Mechanics*, 206:265–297, 1989. doi: 10.1017/S0022112089002302.

Ivar G. Jonsson. Wave boundary layers and friction factors. *Coastal Engineering Proceedings*, 1 (10):127–148, 1966. doi: 10.9753/icce.v10.9.

Michael P. Lamb, Eric A. D'Asaro, and Jeffrey D. Parsons. Turbulent structure of high-density suspensions formed under waves. *Journal of Geophysical Research: Oceans*, 109(C12):C12026, 2004. doi: 10.1029/2004JC002355.

Brian E. Launder and D. Brian Spalding. The numerical computation of turbulent flows. *Computer Methods in Applied Mechanics and Engineering*, 3(2):269–289, 1974. doi: 10.1016/0045-7825(74) 90029-2.

Brian D. Mater and Subhas K. Venayagamoorthy. A unifying framework for parameterizing stably stratified shear-flow turbulence. *Physics of Fluids*, 26(3):036601, 2014. doi: 10.1063/1.4868142.

George L. Mellor and Tetsuji Yamada. A hierarchy of turbulence closure models for planetary boundary layers. *Journal of the Atmospheric Sciences*, 31(7):1791–1806, 1974. doi: 10.1175/ 1520-0469(1974)031⟨1791:AHOTCM⟩2.0.CO;2.

George L. Mellor and Tetsuji Yamada. Development of a turbulence closure model for geophysical fluid problems. *Reviews of Geophysics*, 20(4):851–875, 1982. doi: 10.1029/RG020i004p00851.

Joseph M. Mier, Jordan M. Vetter, Stephen J. Gould, B. M. Sumer, and J. Fredsøe. Coherent structures in oscillatory boundary layers. *Journal of Fluid Mechanics*, 910:A17, 2021. doi: 10.1017/jfm.2020.1002.

John W. Miles. On the stability of heterogeneous shear flows. *Journal of Fluid Mechanics*, 10(4): 496–508, 1961. doi: 10.1017/S0022112061000305.

Walter H. Munk and Ernest R. Anderson. Notes on a theory of the thermocline. *Journal of Marine Research*, 7(3):276–295, 1948.

R. Narasimha and K. R. Sreenivasan. Relaminarization of fluid flows. *Advances in Applied Mechanics*, 19:221–309, 1979. doi: 10.1016/S0065-2156(08)70311-9.

Peter Nielsen. *Coastal Bottom Boundary Layers and Sediment Transport*. World Scientific, Singapore, 1992. doi: 10.1142/1269.

T. R. Osborn. Estimates of the local rate of vertical diffusion from dissipation measurements. *Journal of Physical Oceanography*, 10:83–89, 1980. doi: 10.1175/1520-0485(1980)010⟨0083: EOTLRO⟩2.0.CO;2.

Celalettin E. Ozdemir, Tian-Jian Hsu, and S. Balachandar. A numerical investigation of fine particle laden flow in an oscillatory channel: the role of particle-induced density stratification. *Journal of Fluid Mechanics*, 665:1–45, 2010. doi: 10.1017/S0022112010003769.

Celalettin E. Özdemir, Tian-Jian Hsu, and S. Balachandar. Direct numerical simulations of transition and turbulence in smooth-walled Stokes boundary layer. *Physics of Fluids*, 26(4):045108, 2014. doi: 10.1063/1.4871020.

Stephen B. Pope. *Turbulent Flows*. Cambridge University Press, Cambridge, 2000. doi: 10.1017/CBO9780511840531.

Ludwig Prandtl. Bericht über Untersuchungen zur ausgebildeten Turbulenz. *Zeitschrift für Angewandte Mathematik und Mechanik*, 5(2):136–139, 1925. doi: 10.1002/zamm.19250050212.

Wolfgang Rodi. Examples of calculation methods for flow and mixing in stratified fluids. *Journal of Geophysical Research: Oceans*, 92(C5):5305–5328, 1987. doi: 10.1029/JC092iC05p05305.

S. Salon, V. Armenio, and A. Crise. A numerical investigation of the Stokes boundary layer in the turbulent regime. *Journal of Fluid Mechanics*, 570:253–296, 2007. doi: 10.1017/S0022112006003053.

Pietro Scandura. Steady streaming in a turbulent oscillating boundary layer. *Journal of Fluid Mechanics*, 571:265–280, 2007. doi: 10.1017/S0022112006002965.

Hermann Schlichting and Klaus Gersten. *Boundary-Layer Theory*. Springer, Berlin, 9th edition, 2017. doi: 10.1007/978-3-662-52919-5.

J. F. A. Sleath. Turbulent oscillatory flow over rough beds. *Journal of Fluid Mechanics*, 182:369–409, 1987. doi: 10.1017/S0022112087002374.

Philippe R. Spalart and Barrett S. Baldwin. Direct simulation of a turbulent oscillating boundary layer. *Turbulent Shear Flows*, 6:417–440, 1989. doi: 10.1007/978-3-642-73948-4_32.

George Gabriel Stokes. On the effect of the internal friction of fluids on the motion of pendulums. *Transactions of the Cambridge Philosophical Society*, 9:8–106, 1851.

John R. Taylor and Sutanu Sarkar. Stratification effects in a bottom Ekman layer. *Journal of Physical Oceanography*, 38(11):2535–2555, 2008. doi: 10.1175/2008JPO3934.1.

John R. Taylor, Sutanu Sarkar, and Vincenzo Armenio. Large eddy simulation of stably stratified open channel flow. *Physics of Fluids*, 17(11):116602, 2005. doi: 10.1063/1.2130747.

John H. Trowbridge and Gail C. Kineke. Structure and dynamics of fluid muds on the Amazon continental shelf. *Journal of Geophysical Research: Oceans*, 99(C1):865–874, 1994. doi: 10.1029/93JC02860.

J. S. Turner. *Buoyancy Effects in Fluids*. Cambridge University Press, Cambridge, 1973. doi: 10.1017/CBO9780511608827.

E. R. Van Driest. On turbulent flow near a wall. *Journal of the Aeronautical Sciences*, 23(11):1007–1011, 1956. doi: 10.2514/8.3713.

Giovanna Vittori and Roberto Verzicco. Direct simulation of transition in an oscillatory boundary layer. *Journal of Fluid Mechanics*, 371:207–232, 1998. doi: 10.1017/S002211209800216X.

C. von Kerczek and S. H. Davis. Linear stability theory of oscillatory Stokes layers. *Journal of Fluid Mechanics*, 62(4):753–773, 1974. doi: 10.1017/S0022112074000929.

David C. Wilcox. Reassessment of the scale-determining equation for advanced turbulence models. *AIAA Journal*, 26(11):1299–1310, 1988. doi: 10.2514/3.10041.

Johan C. Winterwerp. Stratification effects by cohesive and noncohesive sediment. *Journal of Geophysical Research: Oceans*, 106(C10):22559–22574, 2001. doi: 10.1029/2000JC000435.

Johan C. Winterwerp. Stratification effects by fine suspended sediment at low, medium, and very high concentrations. *Journal of Geophysical Research: Oceans*, 111(C5):C05012, 2006. doi: 10.1029/2005JC003019.

L. Donelson Wright and Carl T. Friedrichs. Gravity-driven sediment transport on continental shelves: A status report. *Continental Shelf Research*, 26(17–18):2092–2107, 2006. doi: 10.1016/j.csr.2006.07.024.

Francesco Zonta, Miguel Onorato, and Alfredo Soldati. Turbulence and internal waves in stably-stratified channel flow with temperature-dependent fluid properties. *Journal of Fluid Mechanics*, 697:175–203, 2012. doi: 10.1017/jfm.2012.51.